# Real-Time Solar Storm Onset Determination at Lagrange Point 1 (L1) Based on an Optimized Effective Pressure Parameter

*Erik Schmölter and Jens Berdermann*

*Abstract* – The solar storm detection parameter, the effective pressure, which is based on a combination of solar wind velocity and the southward component of the interplanetary magnetic field is investigated with data covering two solar cycles to estimate an optimal configuration for its storm detection capabilities. The implementation of the optimized parameter is able to accurately identify the onset time of solar storms with a false alarm rate of less than 2%, which provides a significantly better performance than, for example, the proton pressure, and has a significant lead time to geomagnetic indices. The effective pressure is further discussed with a selected reference solar storm, showing its potential for storm onset identification.

## 1. Introduction

The interaction between the solar wind and the magnetosphere is a crucial driver of ionospheric disturbances [1]. In particular, time-varying conditions in the solar wind, such as interplanetary coronal mass ejections (CMEs) and corotating interaction regions, with their effect on the coupled ionosphere, thermosphere, and magnetosphere system can have a strong impact on the performance of radio systems used in space-based communication, navigation, and remote sensing. Ionospheric disturbances caused during these space weather effects may degrade the accuracy, reliability, and availability of global navigation satellite systems, such as GPS and the civilian European system Galileo. An understanding of these processes is crucial to implement reliable forecast models and warning systems to assure the undisturbed operation of communication and navigation systems [2]. The storm onset time is essential information for ionospheric models aiming to forecast the solar storm impact. For this purpose, those events and the onsets are considered that are observed at Lagrange point 1 by using satellite measurements and expected to cause an observable geomagnetic storm. Therefore, the effective pressure parameter for real-time ionospheric storm onset detection was introduced in previous studies as part of an ionospheric disturbance forecast model in the European Union Seventh Framework Programme, Advanced Forecast for Ensuring Communication Through Space project [3, 4]. However, at that time, the parameter was never optimized and analyzed for a large sample of solar wind and solar storm conditions. In the present study, the effective pressure is, for the first time, optimized based on solar wind, as well as geomagnetic data covering two solar cycles, showing its potential to determine the onset and strength of an ionospheric storm.

Manuscript received 15 December 2021.

Erik Schmölter and Jens Berdermann are with the German Aerospace Center, Institute for Solar-Terrestrial Physics, Kalkhorstweg 53, 17235 Neustrelitz, Germany; e-mail: Erik.Schmoelter@dlr.de, Jens.Berdermann@dlr.de.

## 2. Data

The solar wind parameters, proton density $n_p$, and proton speed $v_p$, are measured by the Solar Wind Electron, Proton, and Alpha Monitor (SWEPAM) onboard the National Aeronautics and Space Administration (NASA) Advanced Composition Explorer (ACE). The north–south component of the interplanetary magnetic field (IMF) $B_z$ is measured with the magnetic field experiment (MAG) onboard ACE. Both data sets are provided through the NASA ACE Science Center [5].

The disturbance storm time (Dst) and the Kp index are applied to identify geomagnetic storm conditions in the present study [6]. Both parameters are well correlated with solar wind features [7–13] and thus appropriate for the optimization of the proposed effective pressure. Dst measurements are provided by the World Data Center for Geomagnetism (WDC) in Kyoto [14, 15], and Kp measurements are provided by the German Research Centre for Geosciences in Potsdam [16]. All data sets are available from 1998 to 2020 (covering solar cycle 23 and 24) (https://omniweb.gsfc.nasa.gov/form/dx1.html). Therefore, the effective pressure is analyzed for this whole period.

## 3. Calculation of the Effective Pressure

The effective pressure $p_e$ is calculated based on proton density $n_p$, proton speed $v_p$, and north–south component of the IMF $B_z$ according to [3]

$$p_e = \frac{p_d}{e^a + 1}\,[\mathrm{nPa}] \tag{1}$$

with the proton pressure

$$p_d = \frac{1}{2} \cdot n_p \cdot v_p^2\,[\mathrm{nPa}] \tag{2}$$

This proton pressure parameter combines variations of proton density and solar wind velocity (increasing during solar storms) but has several limitations. These include the data availability of $n_p$, which is approxi-

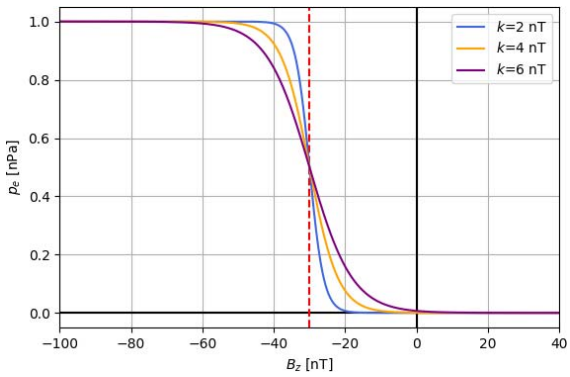


Figure 1. Effective pressure $p_e$ dependent on the north–south component of the IMF $B_z$. The proton pressure $p_d$ is 1 nPa and the threshold $B_{z_0}$ is –25 nT (red dashed line). Three different scaling factors $k$ are illustrated.

mately 64.7% or the detection of only relevant solar storms, because the Earth's impact is also strongly dependent on the optimal coupling of the IMF to the Earth's magnetic field. The function $a$ applied to the Fermi function in (1) is defined as

$$a = \frac{B_z - B_{z_0}}{k} \tag{3}$$

with a threshold $B_{z_0}$ and weighted by a scaling factor $k$. The Fermi function increases $p_e$ with decreasing $B_z$ and reduces $p_e$ with increasing $B_z$. The scaling according to $B_{z_0}$ and $k$ is illustrated in Figure 1. With the presented design, the Fermi function uses $B_z$ to estimate the effectiveness of solar wind energy transfer into the magnetosphere. This is a well-established approach of solar wind–magnetosphere coupling functions [17]. Both parameters $B_{z_0}$ and $k$ may be optimized according to the requirements of specific storm detection algorithms (e.g., best true skill statistic or limited false alarm rate). In the following section, this is implemented for a configuration limited by a false alarm rate of less than 2%. For such a requirement, the effective pressure has several advantages compared with the proton pressure used by most space weather information providers, because it is optimized to detect solar storm onset times for events with strong impact on the Earth ionosphere and radio signals used in navigation and communication services.

## 4. Optimization of the Effective Pressure

Geomagnetic activity with Kp greater than 5 or Dst less than –50 nT is considered as observed solar storm conditions (moderate and strong) for the performance optimization of $p_e$. For this purpose, a time window of 3 h is applied to consider the time delay between occurring solar storms at Lagrange point 1 and the corresponding geomagnetic activity. The actual arrival time of solar wind features varies in time, and geomagnetic activity may occur several hours later, but the selected window seems appropriate for the average response time. In addition, there is no significant

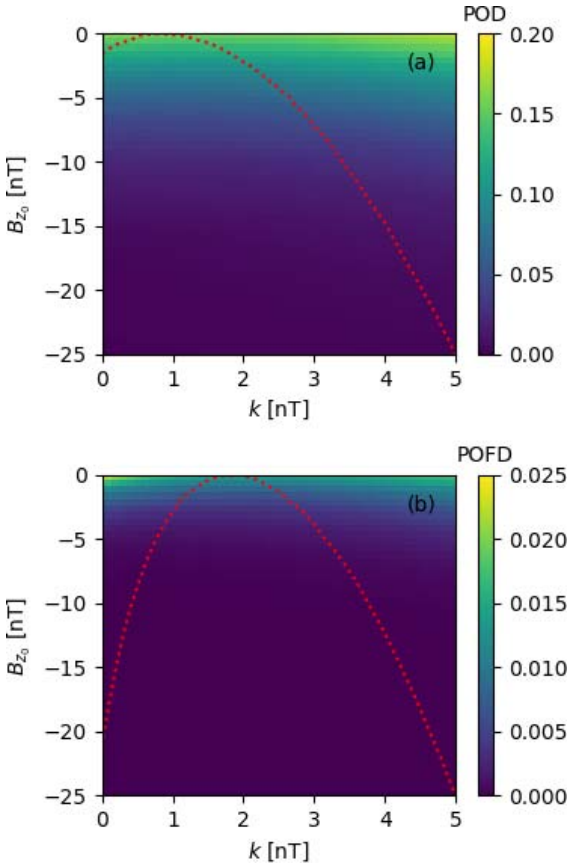


Figure 2. Hit rate (POD) and false alarm rate (POFD) for the solar storm detection based on $p_e$ is illustrated in dependence of threshold $B_{z_0}$ and scaling factor $k$. The mean variation (normalized) of POD and POFD with respect to $k$ is indicated via the red dotted line.

difference in the results and corresponding conclusions for time windows from 1 h to 12 h. For these reasons, this analysis allows us to investigate several events in the analyzed period without manual selection of reference events and corresponding onset times. On the other hand, an expected inaccuracy is introduced due to the procedure because the geomagnetic activity at each storm event is expected to last much longer than the $p_e$ estimated shock of the solar storms (increased number of false negatives). This bias applies to all $p_e$ configurations; therefore, an optimization of $B_{z_0}$ and $k$ can still be performed (relative comparison).

Initial values ranging from –25 nT to 0 nT for $B_{z_0}$ and from 0 nT to 5 nT for $k$ are used to calculate hit and false alarm rates, illustrated in Figure 2. Both performance measurements increase with $B_{z_0}$, but the hit rate in Figure 2a increases much more than the false alarm rate in Figure 2b due to the imbalance of storm and quiet conditions (true positives and true negatives). This indicates that greater values of $B_{z_0}$ have a better performance. However, this is not a satisfactory result, because it removes the distinction between the storm and quiet conditions. The model would be optimized with respect to the hit rate only, which gives too much

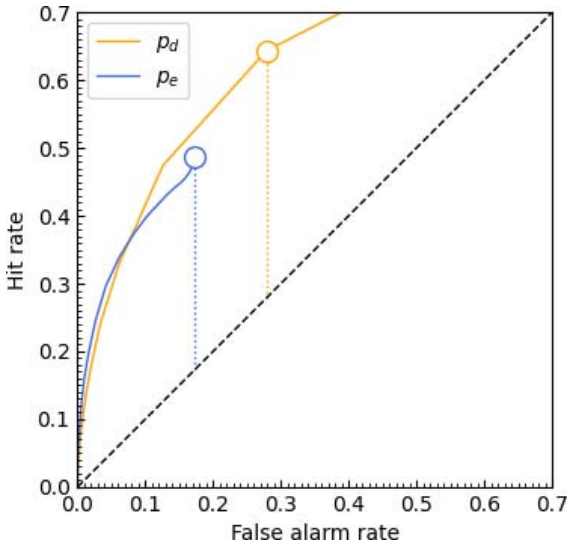


Figure 3. The ROC curves for proton pressure $p_d$ (orange) and effective pressure $p_e$ (blue) are shown. The optimal value for each parameter according to the true skill statistic is marked with corresponding circles and dotted lines. The no-skill condition is marked with a black dashed line.

weight to quiet conditions. For this reason, the variability of both performance measurements is analyzed with respect to $k$. The mean variation of the hit rate (red dotted line in Figure 2a) has a maximum at approximately 1 nT and significantly decreases for greater values. The mean variation of the false alarm rate (red dotted line in Figure 2b) has a maximum at approximately 2 nT and significantly decreases for lesser and greater values. Therefore, an optimal $p_e$ performance is achieved with lesser values of $k$. This information is used to improve the optimization with respect to $B_{z_0}$ by setting $k$ to 0.01 nT in the following analysis.

A receiver operating characteristic (ROC) curve with respect to the hit and false alarm rate is calculated for $p_e$ in comparison to $p_d$. The results are illustrated in Figure 3, showing distinct variations appropriate to analyze the importance of $B_{z_0}$. The optimal performance according to the true skill statistic with respect to $B_{z_0}$ is still biased due to the imbalance of storm and quiet conditions. Additionally, the storm detection performance of $p_e$ is worse than the storm detection performance of $p_d$ according to the true skill statistic. However, these configurations are not sufficient with false alarm rates of 17% and 28%. For the defined false alarm rate limit of 2% (and for false alarm rates up to 7.5%), the hit rate of $p_e$ is better; thus, its solar storm detection performance is better compared with $p_d$ (see Figure 3). This preferred range corresponds to values of $B_{z_0}$ smaller than –4.5 nT, and a value of –10.6 nT satisfies the defined false alarm rate limit. Thus, both parameters $B_{z_0}$ and $k$ can be optimized.

The optimal configuration estimates approximately 900 storm onsets in the analyzed period. This is a satisfactory result considering the selected time window

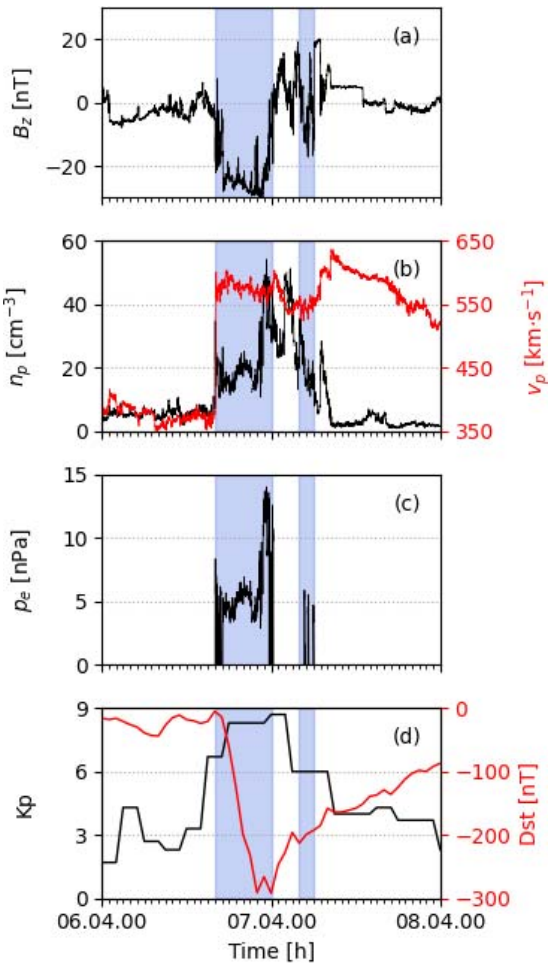


Figure 4. North–south component of the IMF $B_z$ (a), proton density $n_p$ and proton speed $v_p$ (b), effective pressure $p_e$ (c), and Kp and Dst (d) are shown for the CME during April 6, 2000. The blue shading indicates the periods that are considered storm conditions according to $p_e$.

of 3 h and data gaps. In future studies, these could be compared with reference lists or examined in detail. Nevertheless, for such a large number of events, an automated analysis, as applied in the present study, is required too.

## 5. CME Detection Using the Effective Pressure

The solar storm detection using $p_e$ is illustrated with the CME during April 6, 2000, in Figure 4. Proton density $n_p$ and proton speed $v_p$ in Figure 4b show the shock at 16:00 UTC with a strong increase for both solar wind parameters. The north–south component of the IMF $B_z$ in Figure 4a shows a strong decrease during this period, with values below the optimized threshold $B_{z_0}$. A weaker decrease of $B_z$ is observed at 04:00 UTC during the next day, and $B_{z_0}$ is only partially exceeded. Nonetheless, the respective time periods are also observed for $p_e$ in Figure 4c, but there is a more well-

defined difference between the storm and quiet conditions. This is due to the contribution of the scale $a$ [see (3)], which, on the one hand, causes $p_e$ values of 0 for quiet conditions, but, on the other hand, is not categorical (see smooth transitions due to $k$ in Figure 1). Increased $n_p$ and $v_p$ are sufficient to cause an increase of $p_e$, while $B_z$ is not significantly greater than $B_{z_0}$. The blue shading (storm conditions according to $p_e$) in Figure 4d correlate well with the onset of geomagnetic activity according to Kp and Dst. However, the explained gap in the period is observed, and the recovery phase is not identified as storm conditions, as expected (discussed in the previous section). Nevertheless, the example gives an impression of the variability of $p_e$ during a solar storm.

## 6. Conclusion and Outlook

The effective pressure $p_e$, was investigated in the present study and optimized based on solar wind data covering two solar cycles. A configuration with optimal performance (false alarm rate of less than 2%), based on the comparison of $p_e$ storm detection results and the observed geomagnetic activity (Kp or Dst), was estimated. A $B_z$ theshold $B_{z_0}$ of approximately −10 nT and a scaling factor $k$ of 0.01 nT [see (3)] was identified for $p_e$ [see(1)] optimization, outperforming the commonly used proton pressure $p_d$ (see Figure 3). In addition, $p_e$ is able to identify quiet conditions with respect to the ionospheric impact, identified with a value of zero, and can therefore clearly separate between different storm conditions (see Figure 4).

The solar storm detection using the effective $p_e$ allows us to identify the corresponding onset time needed for reliable model-based forecasts of ionospheric conditions. In the future, the parameter needs to be applied to empirical and physical ionospheric models to forecast space weather impact based on real-time measurements. The presented results of the optimized effective pressure provide an advancement for the forecast of space weather impacts. However, an extended analysis and improved optimization of the effective pressure in the future might lead to further improvements.

## 7. Acknowledgments

We thank the ACE MAG and SWEPAM instrument team and the ACE Science Center for providing the ACE data, the German Research Centre for Geosciences Potsdam for providing Kp index data, and WDC Kyoto for providing Dst index data.

## 8. References

1. S. E. Milan, L. B. N. Clausen, J. C. Coxon, J. A. Carter, M.-T. Walach, et al., "Overview of Solar Wind–Magnetosphere–Ionosphere–Atmosphere Coupling and the Generation of Magnetospheric Currents," *Space Science Reviews*, **206**, 1–4, February 2017, pp. 547-573.
2. J. P. Eastwood, E. Biffis, M. A. Hapgood, L. Green, M. M. Bisi, et al., "The Economic Impact of Space Weather: Where Do We Stand?" *Risk Analysis*, **37**, 2, February 2017, pp. 206-218.
3. C. Borries, J. Berdermann, N. Jakowski, M. Hoque, and V. Bothmer, "Preparation of an Advanced TEC Forecast Based on the Statistical Analysis of Historical Ionospheric Storms," 4th International Galileo Science Colloquium, Prague, Czech Republic, December 4–6, 2013.
4. C. Borries, J. Berdermann, N. Jakowski, and V. Wilken, "Ionospheric storms–A challenge for Empirical Forecast of the Total Electron Content," *Space Science Reviews*, **120**, 4, March 2015, pp. 3175-3186.
5. T. L. Garrard, A. J. Davis, J. S. Hammond, and S. R. Sears, "The ACE Science Center," *Space Science Reviews*, **86**, 1/4, 1998, pp. 649-663.
6. P. N. Mayaud, *Derivation, Meaning, and Use of Geomagnetic Indices*, Washington, DC, American Geophysical Union, 1980.
7. J. A. Valdivia, A. S. Sharma, and K. Papadopoulos, "Prediction of Magnetic Storms by Nonlinear Models," *Geophysical Research Letters*, **23**, 21, October 1996, pp. 2899-2902.
8. J.-G. Wu and H. Lundstedt, "Prediction of Geomagnetic Storms From Solar Wind Data Using Elman Recurrent Neural Networks," *Geophysical Research Letters*, **23**, 4, February 1996, pp. 319-322.
9. F. Boberg, P. Wintoft, and H. Lundstedt, "Real Time Kp Predictions From Solar Wind Data Using Neural Networks," *Physics and Chemistry of the Earth, Part C: Solar, Terrestrial & Planetary Science*, **25**, 4, April 2000, pp. 275-280.
10. T. P. O'Brien and R. L. McPherront, "Forecasting the Ring Current Index Dst in Real Time," *Journal of Atmospheric and Solar-Terrestrial Physics*, **62**, 14, September 2000, pp. 1295-1299.
11. F. Boberg, P. Wintoft, and H. Lundstedt, "A New Model for the Prediction of Dst on the Basis of the Solar Wind," *Journal of Geophysical Research: Space Physics*, **107**, A12, 2002, pp. SMP 31–1–SMP 31–8.
12. R.-S. Kim, Y.-J. Moon, N. Gopalswamy, Y.-D. Park, and Y.-H. Kim, "Two-Step Forecast of Geomagnetic Storm Using Coronal Mass Ejection and Solar Wind Condition," *Space Weather*, **12**, 4, April 2014, pp. 246-256.
13. P. Wintoft, M. Wik, J. Matzka, and Y. Shprits, "Forecasting Kp From Solar Wind Data: Input Parameter Study Using 3-Hour Averages and 3-Hour Range Values," *Journal of Space Weather and Space Climate*, **7**, November 2017, p. A29.
14. M. Sugiura and T. Kamei, *Equatorial Dst Index 1957–1986*, Paris, ISGI Publications Office, 1991.
15. M. Nose, M. Sugiura, T. Kamei, T. Iyemori, and Y. Koyama, "Dst Index," Kyoto, World Data Center for Geomagnetism, 2015. Access via http://dx.doi.org/10.17593/14515-74000 or http://isgi.unistra.fr/indices_dst.php (last access: 07.03.2022)
16. J. Matzka, O. Bronkalla, K. Tornow, K. Elger, and C. Stolle, "Geomagnetic Kp Index, version. 1.0," Potsdam, Germany, German Research Centre for Geosciences Data Services, 2021. Access via https://doi.org/10.5880/Kp.0001 or https://dataservices.gfz-potsdam.de/panmetaworks/showshort.php?id=escidoc:5216888 (last access: 07.03.2022).
17. W. D. Gonzalez, "A Unified View of Solar Wind-Magnetosphere Coupling Functions," *Planetary and Space Science*, **38**, 5, May 1990, pp. 627-632.